1 Measurement Preparation

1.1 Surface Roughness Measurement

Roughness profiles of the foiled (f) and unfoiled (unf) surfaces of the test rig (cf. Sec. 2.2 in the main manuscript) were measured to assess the need for consideration in CFD simulations, see Fig. 1. The measurements have been performed on a stationary MarSurf roughness system equipped with a GD 25 traverse unit and a BFW stylus, controlled via MarTalk. Measured profiles were filtered using a Gaussian short-wavelength filter (S-filter) with cutoff $L_s = 2.5\,\mu\text{m}$ and a Gaussian roughness filter (C-filter) with cutoff $\lambda_c = 0.8\,\text{mm}$, in accordance with ISO 16610 [1]. The total trace length corresponded to $L_t = 5.6\,\text{mm}$, with an evaluation length of $L_n = 4\,\text{mm}$ as defined in ISO 21920 [2].

Using the algorithm of Adams et al. [3] the equivalent sandgrain roughness estimated from the arithmetical mean roughness value, averaged over the three measured profiles for the foiled surfaces in Fig. 1a, results in $\varepsilon(\bar{R}_{a,\text{f}}) = 3.15\,\mu\text{m}$ and for the unfoiled surfaces (Fig. 1b) in $\varepsilon(\bar{R}_{a,\text{unf}}) = 35.5\,\mu\text{m}$.

Taking the velocity profiles of the dashboard-attaching jet (see Appendix B in the main manuscript) as a basis and applying the Bradshaw-Gee fit [4] for a planar turbulent wall-jet, defined as:

$$\text{Re}_\text{c} = \frac{U_\text{c}\, y_\text{c}}{\nu}, \qquad C_{f,\text{c}} = 0.0315\, Re_\text{c}^{-0.182}, \qquad u_\tau = U_\text{c}\sqrt{\frac{C_{f,\text{c}}}{2}}, \tag{1}$$

the viscous sublayer thickness can be estimated roughly as $\delta_\text{vsl} = 3\frac{\nu}{u_\tau} \approx 0.2\text{-}0.3\,\text{mm} \gg \varepsilon(\bar{R}_a)$. In Eq. 1 quantities indexed with c refer to the jet centerline: $U_\text{c} = \langle|\boldsymbol{U}|\rangle\,(\eta, \xi = 0)$ and $y_\text{c} = y\,(U_\text{c})$. The factor of 3 in the viscous sublayer thickness estimation takes into account its extend in wall jets [5], as opposed to a value of $\delta_\text{vsl} = 5\frac{\nu}{u_\tau}$, generally used for channel flows [6]. This assessment shows that the flow can be considered hydraulically smooth.

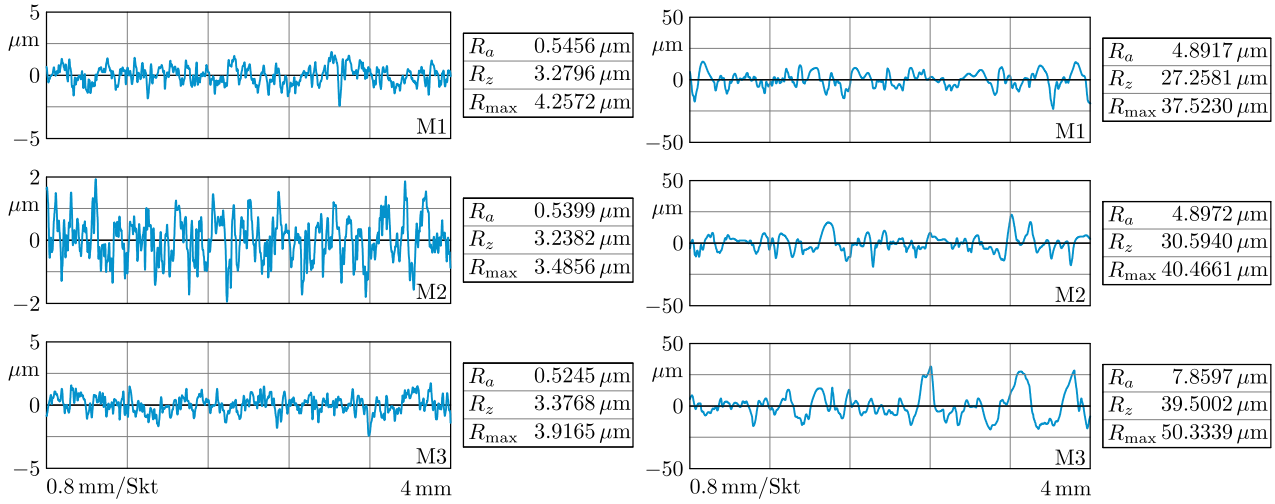

(a) Foiled surfaces. (b) Unfoiled surfaces.

Supp. Fig. 1: Surface roughness measurements.

1.2 Test Rig 3D Scan

In preparation for the measurement campaign, the primary defrost duct was partially digitized using a combination of structured-light projection and photogrammetry.

In photogrammetry, overlapping photographs (e.g., acquired with a digital single lens reflex camera) taken from multiple viewpoints are processed to estimate the camera poses. Image features are then matched across views and used to triangulate their 3D positions, yielding a 3D point cloud. Since the test rig surfaces are comparatively smooth and featureless, reference markers and a self-vanishing spray were applied to introduce a high-contrast, non-repeating pattern, improving feature matching and the resulting surface reconstruction.

For structured-light projection, the primary defrost duct was scanned with an ATOS Core 300 fringe-projection system with an uncertainty of 0.06 mm, in which a projector casts calibrated (blue) fringe patterns onto the surface and stereo cameras record the pattern deformation to compute dense 3D surface points via triangulation. Successive views are then registered into a common coordinate system to obtain a complete surface model.

The main results of the scan are summarized in Fig. 2. The surface deviation from a fitted plane in Fig. 2a shows that the maximum deviation occurs in the area of the acrylic glass bridge on the side of the optical access of the PIV cameras. Nevertheless, the deviations are within an acceptable range considering the spanwise extend of 1 m of the defrost duct, with a maximum difference relative to the average measured duct width of 5.5% for the duct width in x direction (cf. Fig. 2c) and 6.8% for the exit edge flushness in y direction (cf. Fig. 2d).

As is explained in Sec. 1.3, the angle of the primary defrost duct β can be derived from the turning angle of the rotary disk γ using trigonometric relationships. However, this requires knowing at least one value of β precisely to eliminate γ as an unknown. This value was extracted from the 3D scan, as shown in Fig. 2b. For this purpose, the duct angle was set to its maximum position before the scan, which is determined by the physical stop (cf. Sec. 2.1 in the main manuscript), using the robotic arm. The angle can then be obtained graphically or from the triangulated surface model using suitable CAD software and results in $\beta_{\max} = 84.9°$.

1.3 Determination of the Primary Duct Angle

To obtain an analytical formula for the angle of the primary duct β in terms of the turning angle γ of the rotary disk which connects to the cobot (cf. Fig. 2b in the main manuscript), the following geometric relationships are derived from Fig. 3a

$$\begin{aligned} L_4 \cos\delta &= l\cos\beta + L_3 + r\cos\gamma, \\ L_4 \sin\delta &= H - r\sin\gamma - l\sin\beta, \end{aligned} \tag{2}$$

with the known parameter values given as:

$$r = 34.25\,\text{mm}, \qquad l = 40\,\text{mm}, \qquad H = 73.64\,\text{mm}, \qquad L_3 = 516\,\text{mm}, \qquad L_4 = 540\,\text{mm}.$$

Using the identity $\cos^2\delta + \sin^2\delta = 1$, squaring and adding of Eq. (2) to eliminate δ, results in

$$L_4^2 = \left(l\cos\beta + L_3 + r\cos\gamma\right)^2 + \left(H - r\sin\gamma - l\sin\beta\right)^2. \tag{3}$$

Expanding the squared brackets in Eq. (3), together with defining

$$A \coloneqq L_3 + r\cos\gamma, \quad B \coloneqq H - r\sin\gamma, \quad C \coloneqq \frac{L_4^2 - l^2 - A^2 - B^2}{2l},$$

yields the expression

$$A\cos\beta - B\sin\beta = C. \tag{4}$$

Since $A > 0$ and $B > 0$, we further define $R \coloneqq \sqrt{(A^2 + B^2)}$ and $\varphi \coloneqq \operatorname{arctan2}(B, A)$, such that A/R and B/R correspond to points on a unit circle:

$$\left(\frac{A}{R}\right)^2 + \left(\frac{B}{R}\right)^2 = 1, \quad A = R\cos\varphi, \quad B = R\sin\varphi, \tag{5}$$

with arctan2 being the two-argument arctangent, which returns unambiguous values for the angle between the positive abscissa and a line from the origin to the point (A, B). Applying the cosine addition theorem $\cos(\varphi + \beta) = \cos\varphi\cos\beta - \sin\varphi\sin\beta$ and comparing with Eq. (4), we find

$$R\cos(\varphi + \beta) = C,$$

and arrive at an expression for β in terms of the rotary disk angle γ

$$\beta = -\varphi \pm \arccos\frac{C}{R} + 2k\pi, \quad k \in \mathbb{Z}. \tag{6}$$

Since in our case $0 < \beta < \pi/2$, only positive branch solutions are valid.

Together with the initial value for $\gamma_{\min}$, determined from the known value of $\beta_{\max}$ taken from the 3D-scan (cf. Sec. 1.2), the required primary duct angles can be calculated using Eq. (6) down to the lower stop value $\beta_{\min} = 42.6°$ for any angular position of the rotary disk controlled by the robotic arm, as depicted by the line plot in Fig. 3b.

The primary duct angle can alternatively be determined using the raw images from the PIV measurements. Since the laser sheet illuminates the duct from above, a sharp contrast relative to the dark background is created

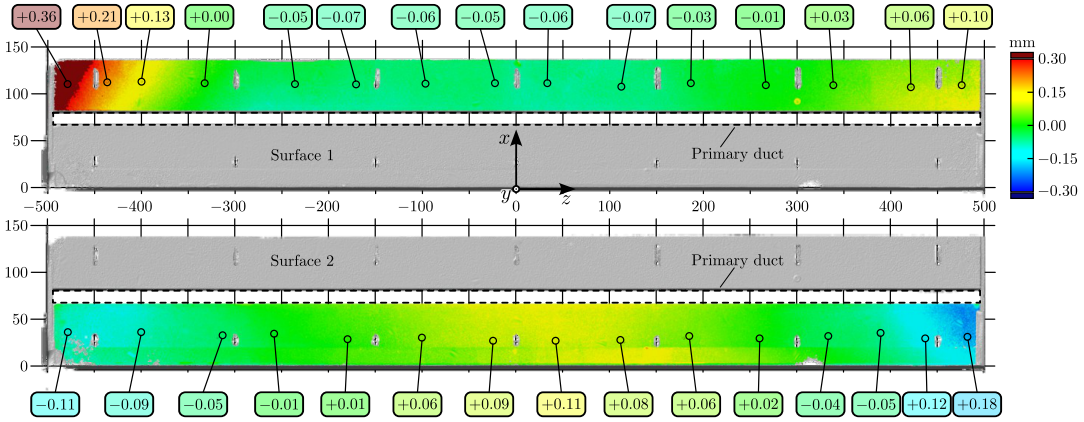

(a) Surface deviation from respective fitted plane.

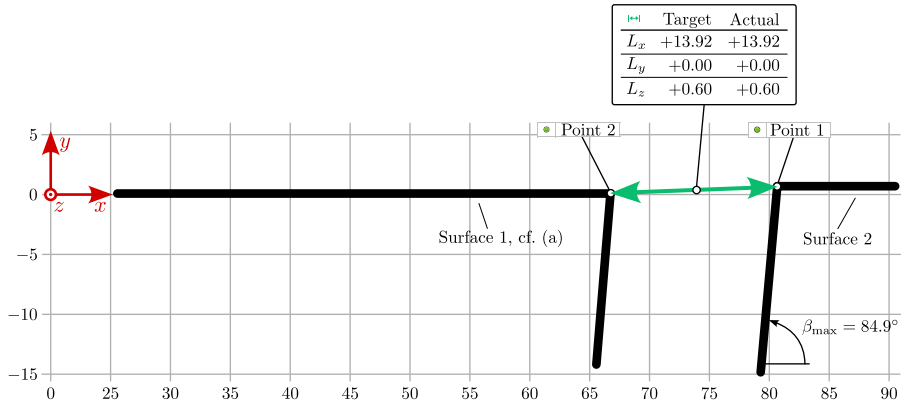

(b) Duct exit edge distances in mid-plane ($z = 0$).

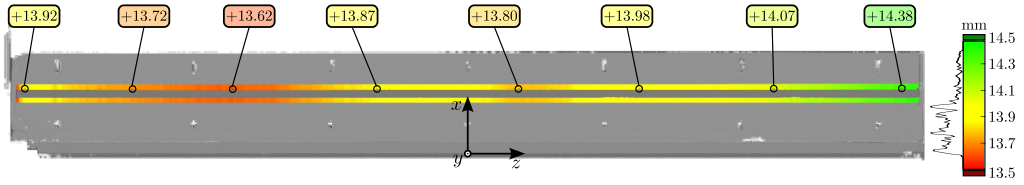

(c) Duct width (in x) variation along spanwise direction.

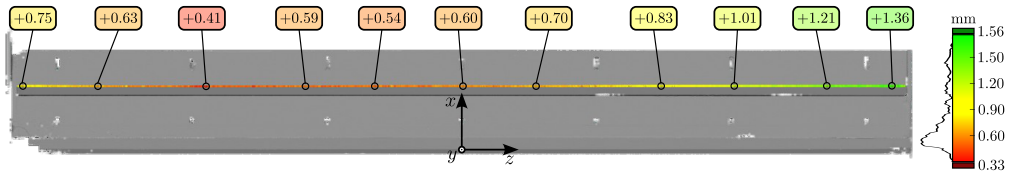

(d) Duct exit edge flushness (in y) variation along spanwise direction.

Supp. Fig. 2: Results of the primary duct 3D scan.

in the particle image when the laser light exits at the duct entrance. A sample comparison for the three angles displayed in Fig. 3 carried out against this method validates the geometric determination of the duct angle.

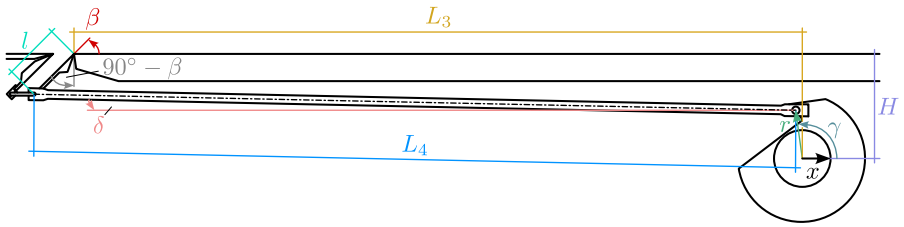

(a) Parameters of the angle adjustment mechanism.

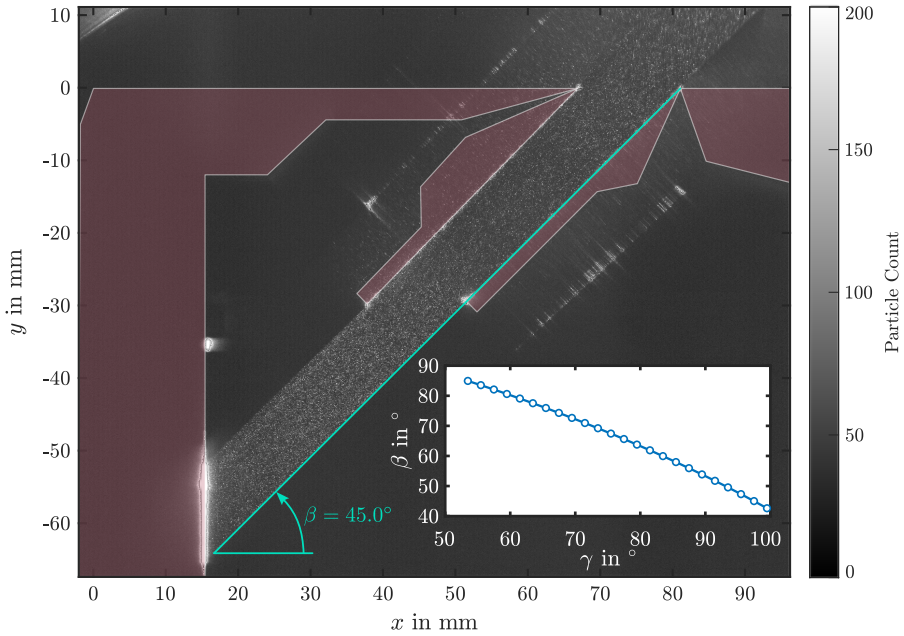

(b) Measurement of the primary duct angle using the raw PIV image for rotary disk angle $\gamma = 97.5°$. The line plot shows the relation $\beta(\gamma)$ of Eq. (6) over the complete range of realizable γ-values.

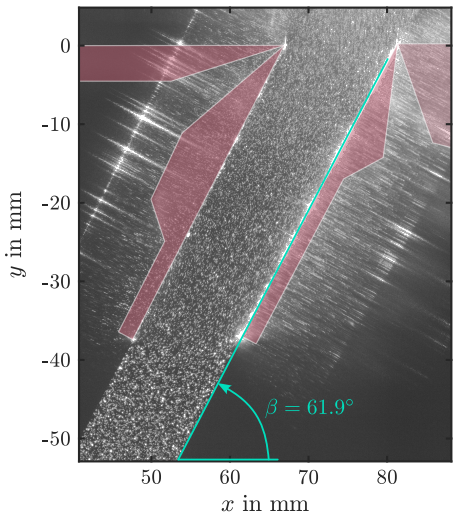

(c) $\gamma = 81.5°$

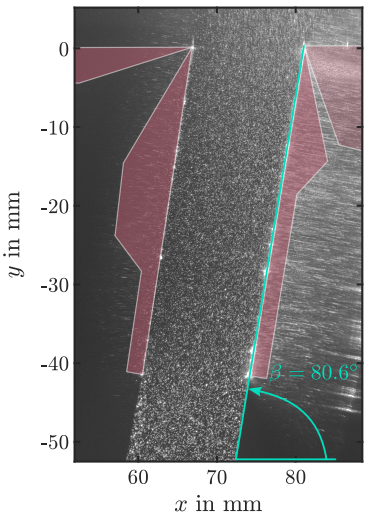

(d) $\gamma = 59.5°$

Supp. Fig. 3: Determination of the primary duct angle.

1.4 PIV Convergence Studies

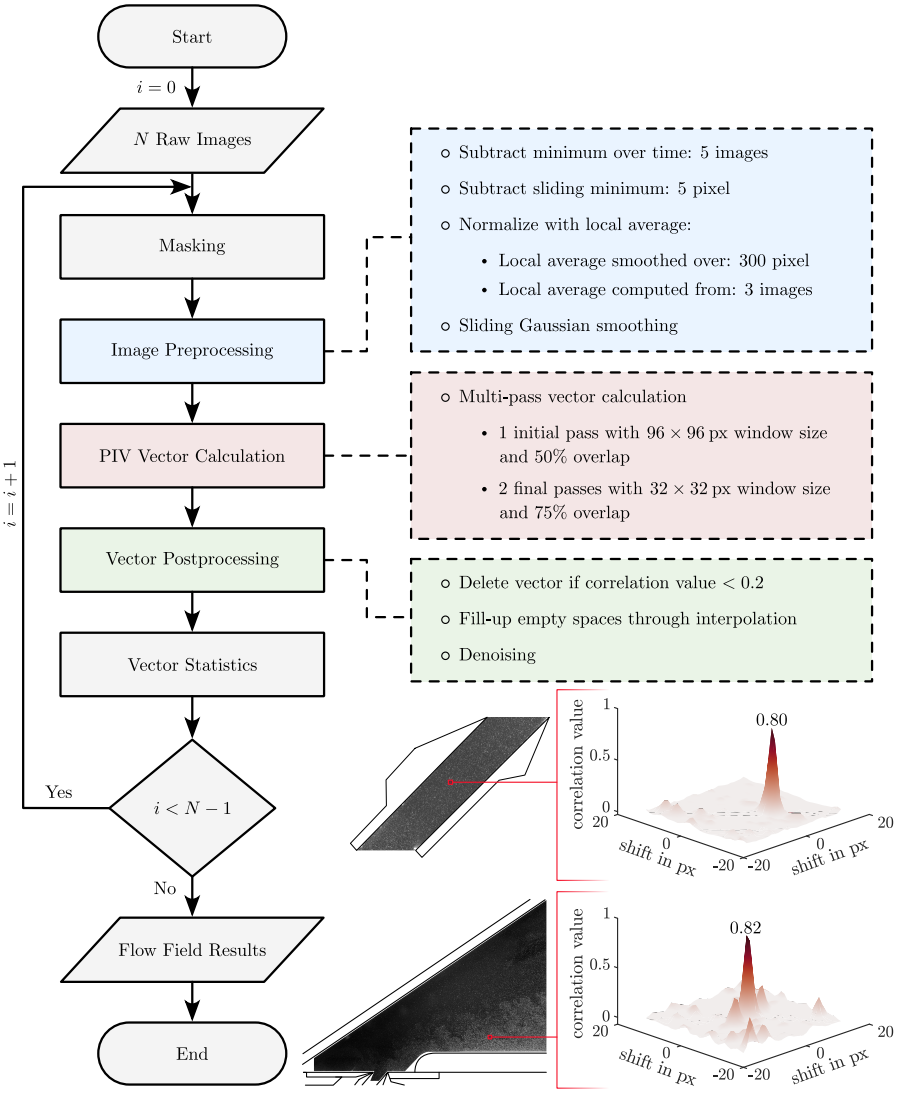

Supp. Fig. 4: Flowchart of the PIV pre- and postprocessing steps. Bottom right: Exemplary snapshots of tracer distribution within ROI 2 and ROI 3 with corresponding correlation maps for a (32×32) px window size.

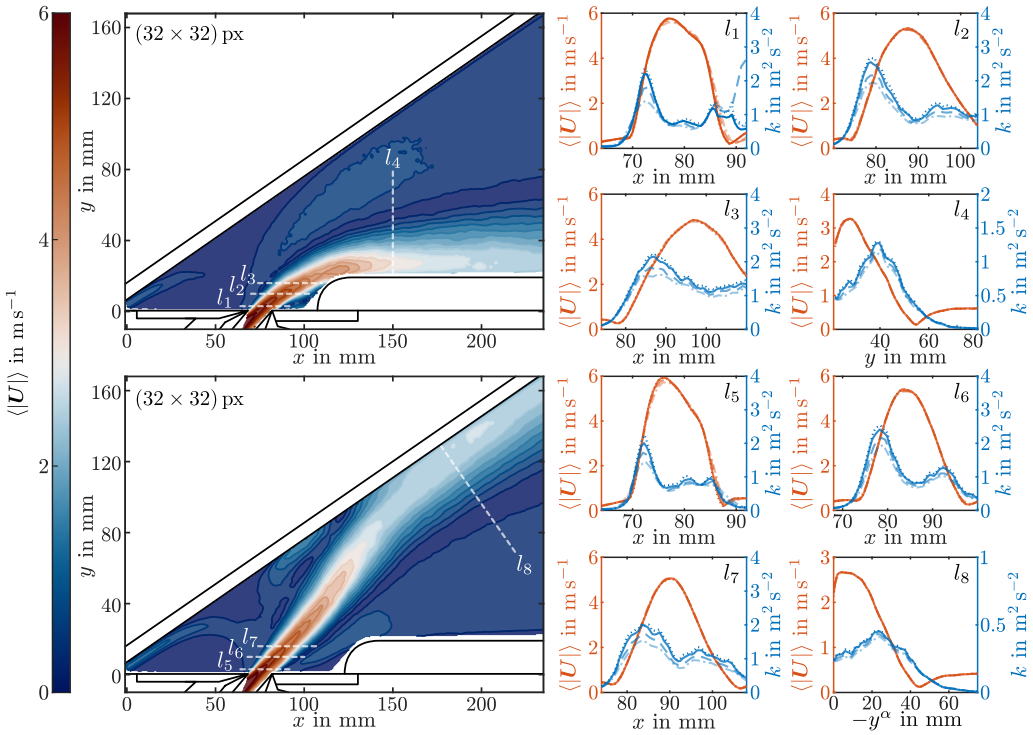

(a)

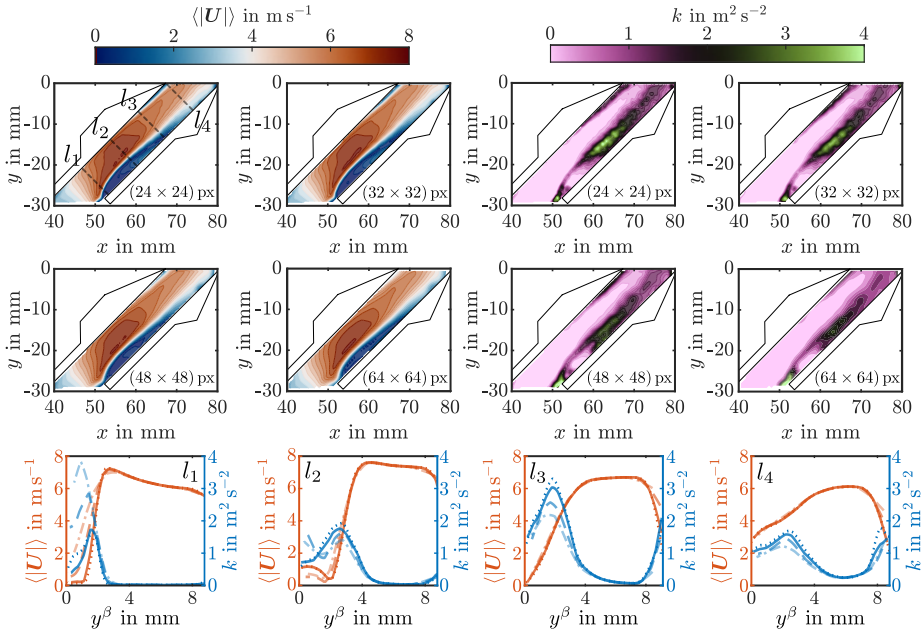

(b)

Supp. Fig. 5: Effect of the correlation window size on time-averaged velocity magnitude and turbulent kinetic energy evaluated using 100 PIV samples for $\beta = 45°$ and $L_s = 24\,\mathrm{mm}$ (top)—$L_s = 40\,\mathrm{mm}$ (bottom). **(a)** Jet near field (ROI 2, cf. figure 3c in the main manuscript). **(b)** Primary duct (ROI 3). ┅ | ┅ (24×24) px, ━ | ━ (32×32) px, ╍ | ╍ (48×48) px, ┈ | ┈ (64×64) px.

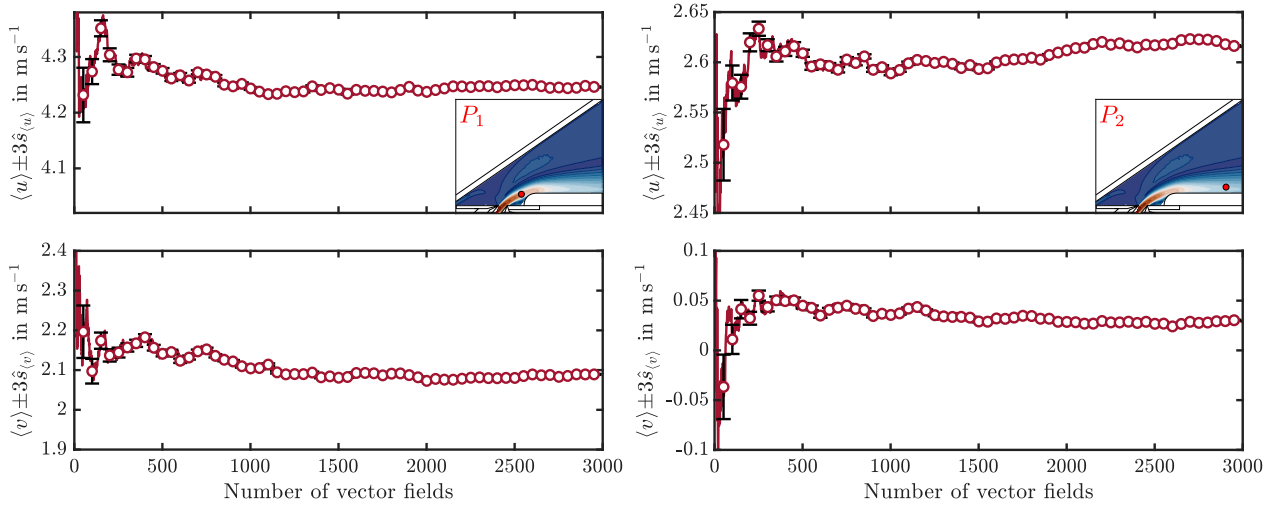

(a)

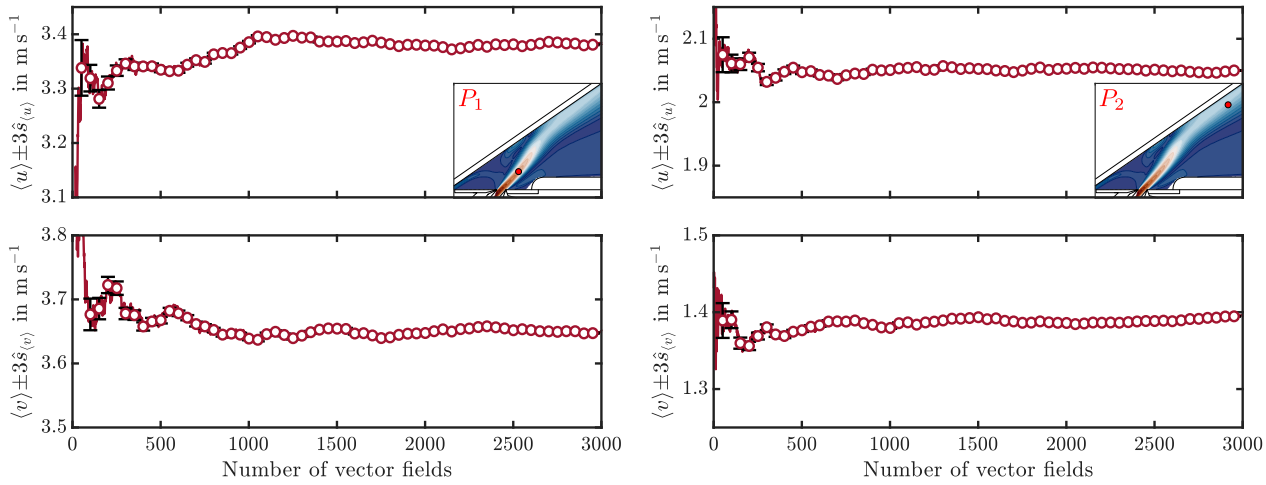

(b)

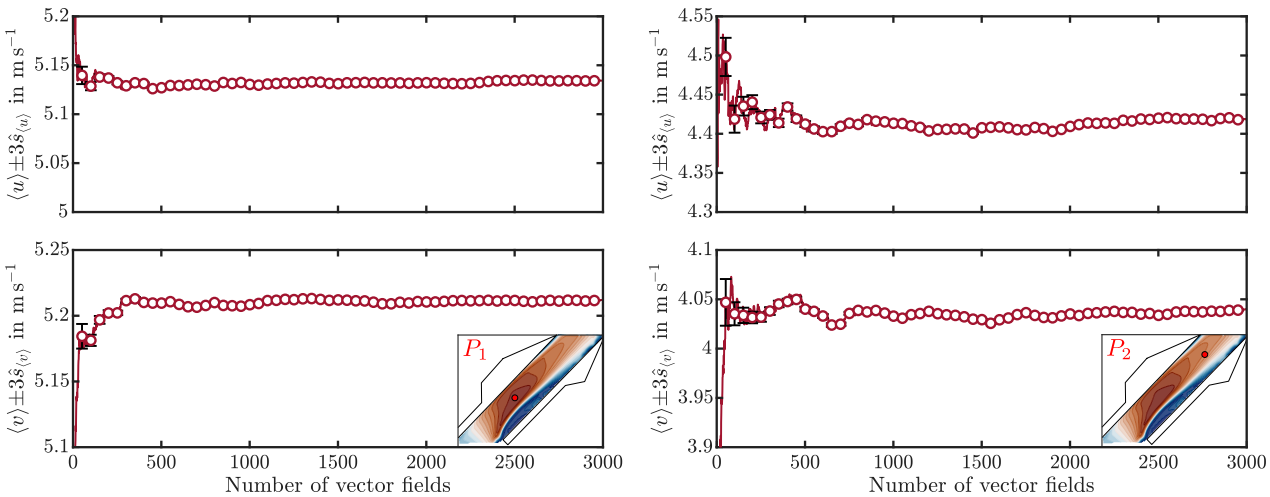

(c)

Supp. Fig. 6: Cumulative average of the in plane velocity components demonstrating statistical convergence with increasing number of PIV samples. Error bars denote ±3× standard error of the mean, corresponding approximately to a 99.7% confidence interval under the assumption of normally distributed, uncorrelated samples. Uncertainty bounds become smaller than the marker size with increasing number of vector fields. **(a)** $(x_1|y_1) = (104.2|19.3)$ mm. $(x_2|y_2) = (211.3|32.2)$ mm. **(b)** $(x_1|y_1) = (101.6|29.0)$ mm. $(x_2|y_2) = (210.4|137.5)$ mm. **(c)** $(x_1|y_1) = (54.7|-18.3)$ mm. $(x_2|y_2) = (68.1|-4.0)$ mm.

2 Determination of the Inflow Conditions

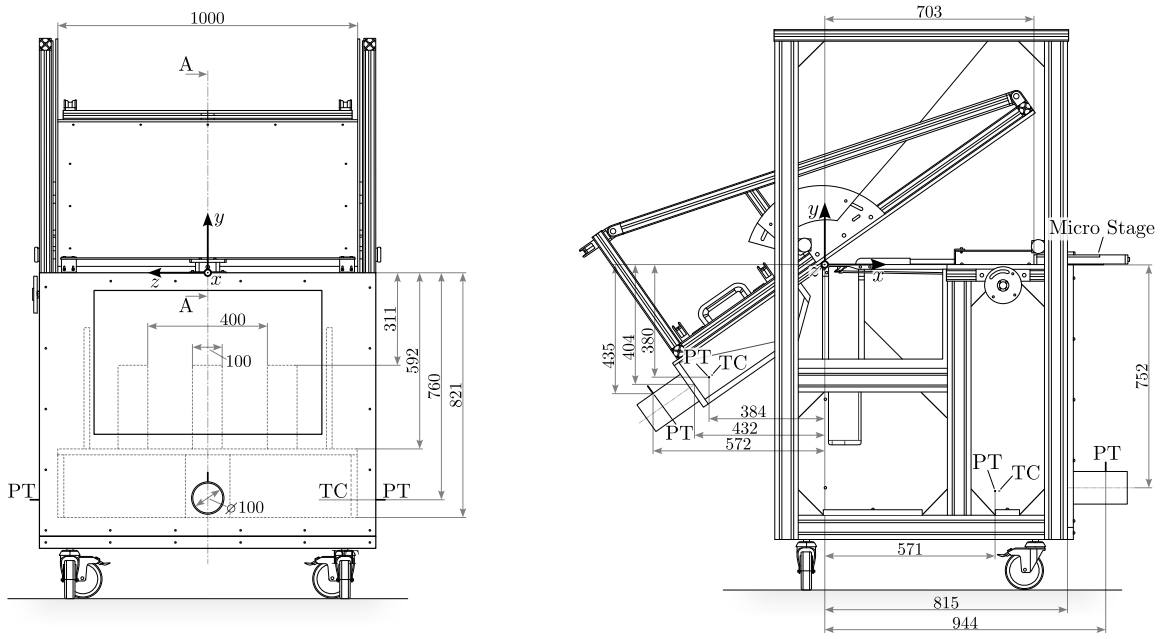

(a) (b)

Supp. Fig. 7: Front and side view with relevant test rig dimensions including thermocouple (TC) and pressure tap (PT) positions.

Supp. Tab. 1: PIV imaging and acquisition setup for the inflow condition measurements.

	Model — Value	
Instrument — Parameter	**Primary inflow section**	**Secondary inflow section**
Camera	LaVision Imager CX1-12	LaVision Imager CX1-12
Lens (mount)	Nikon AF 60 mm 2.8 D Micro	Nikon AF 60 mm 2.8 D Micro
Aperture f/#	f/4	f/4
Object distance	~ 1600 mm	~ 1600 mm
Calibration/scaling method	2D calibration plate	2D calibration plate
Calibration target	134-12 SSSP	134-12 SSSP
Scale factor	$14.58\,\mathrm{px\,mm^{-1}}$	$15.54\,\mathrm{px\,mm^{-1}}$
Pixel size in object space	$68.6\,\mu\mathrm{m\,px^{-1}}$	$64.4\,\mu\mathrm{m\,px^{-1}}$
Correlation window (final pass)	32×32 px	32×32 px
Window overlap (final pass)	75%	75%
Particle image density	0.024–0.036 ppp	0.047–0.065 ppp
Number of image-pairs N	2500	4500
Repetition rate f_r	15 Hz	2 Hz
Pulse separation dt	2 ms	10 ms

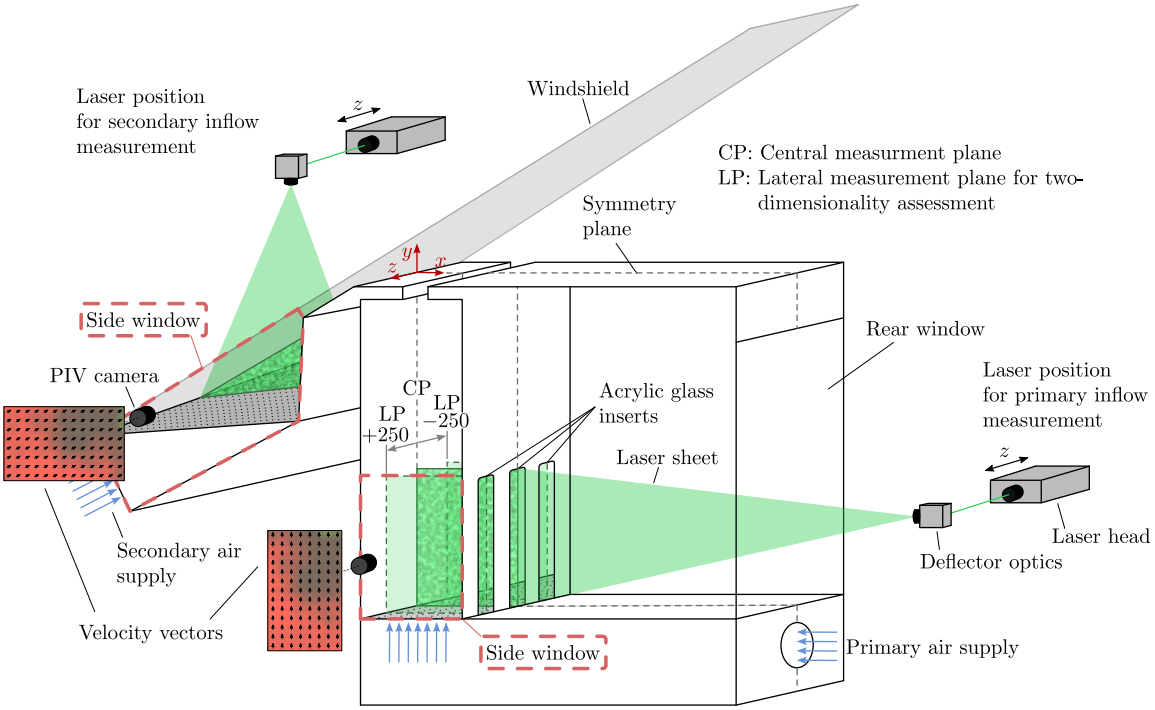

Supp. Fig. 8: Schematic depiction of the inflow measurement procedure (not true to scale). Besides the symmetry plane, additional measurements are carried out for two-dimensionality assessment at planes distributed along the spanwise direction.

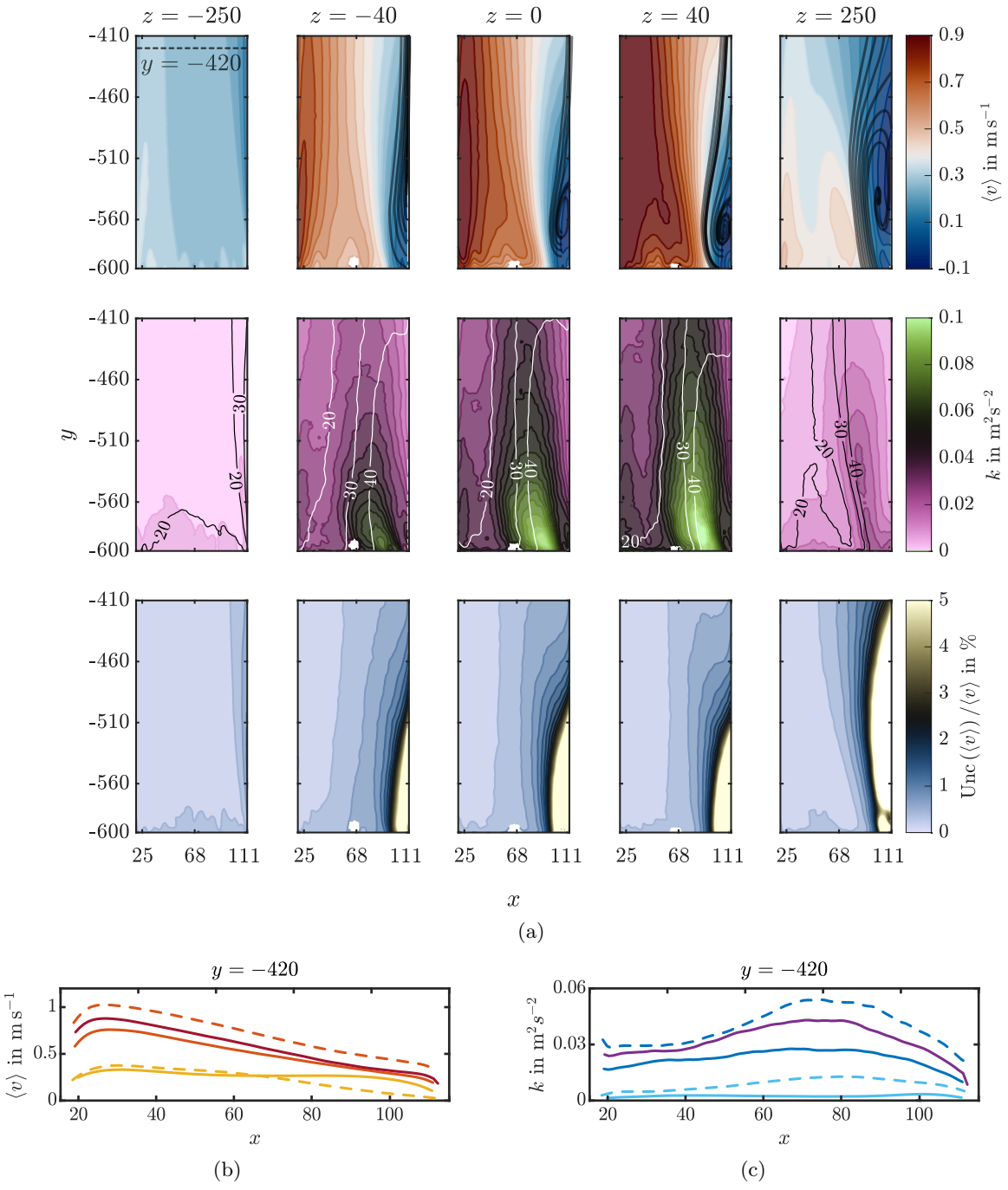

Supp. Fig. 9: Primary duct inflow conditions in measurement planes distributed along the spanwise direction (cf. figure 8). **(a)** Top row: Time-averaged y-velocity component $\langle v \rangle$ with superimposed streamlines (black) indicating separation region. Mid row: Corresponding turbulent kinetic energy. Contour-lines represent turbulence intensity levels $\sqrt{\frac{2}{3}k}/\langle |\boldsymbol{U}| \rangle$ in %. Bottom row: $\langle v \rangle$ uncertainty estimation. All statistics have been obtained using 2500 PIV samples. **(b) & (c)** $\langle v \rangle$ and k evaluated at $y = -420\,\mathrm{mm}$ (dashed line in (a)). — | — $z = -250$, — | — $z = -40$, — | — $z = 0$, — | — $z = 40$, — | — $z = 250$. **Spatial units:** $[x] = [y] = [z] = \mathrm{mm}$.

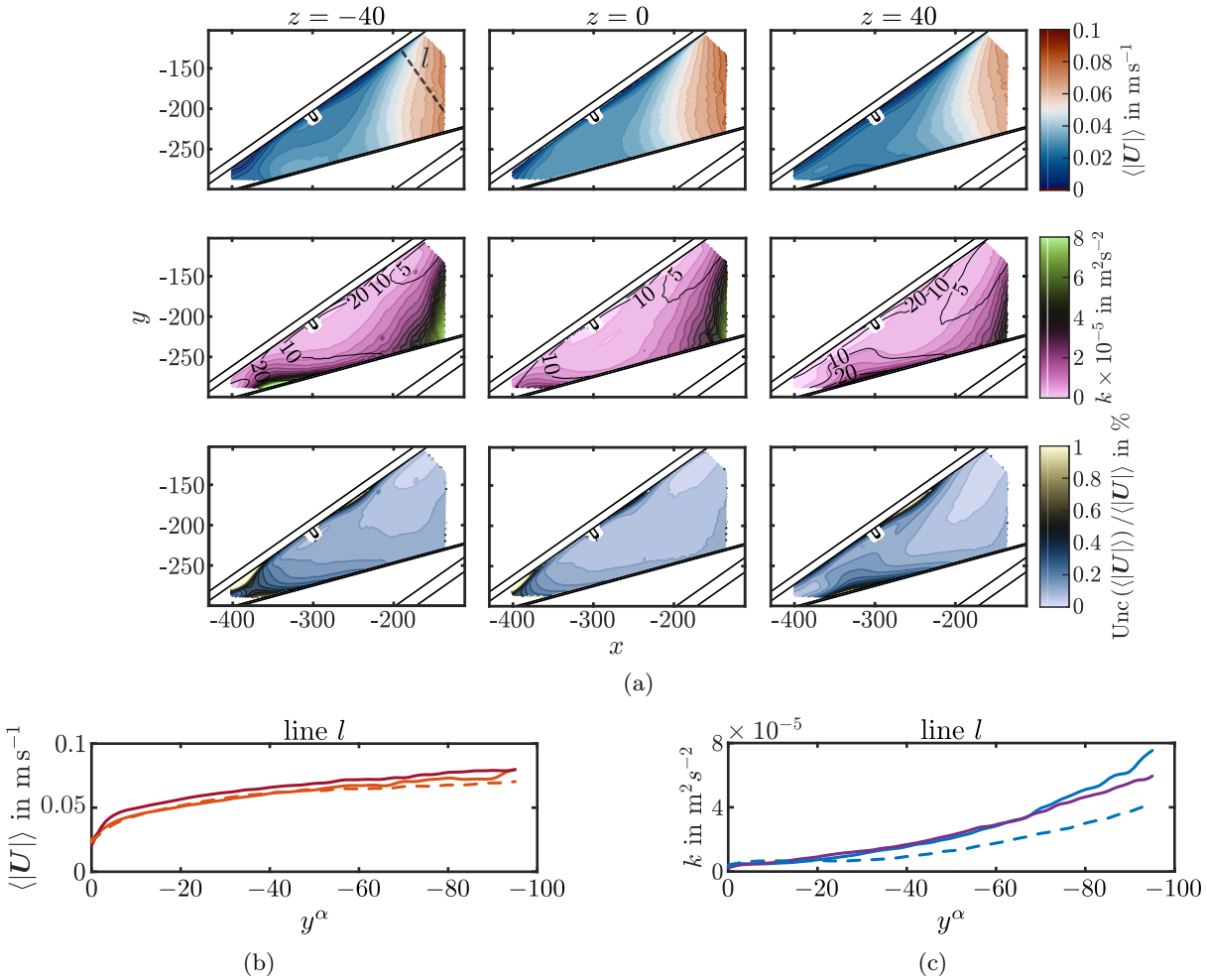

Supp. Fig. 10: Secondary duct inflow conditions in measurement planes distributed along the spanwise direction. **(a)** Top row: Time-averaged velocity magnitude. Mid row: Corresponding turbulent kinetic energy. Contour-lines represent turbulence intensity levels $\sqrt{\frac{2}{3}k}/\langle|\boldsymbol{U}|\rangle$ in %. Bottom row: $\langle|\boldsymbol{U}|\rangle$ uncertainty estimation. All statistics have been obtained using 4500 PIV samples. **(b) & (c)** $\langle|\boldsymbol{U}|\rangle$ and k evaluated along dashed line in (a). — | — $z = -40$, — | — $z = 0$, - - | - - $z = 40$. **Spatial units:** $[x] = [y] = [z] =$ mm.

3 Two-Dimensionality Assessment of the Flow Field

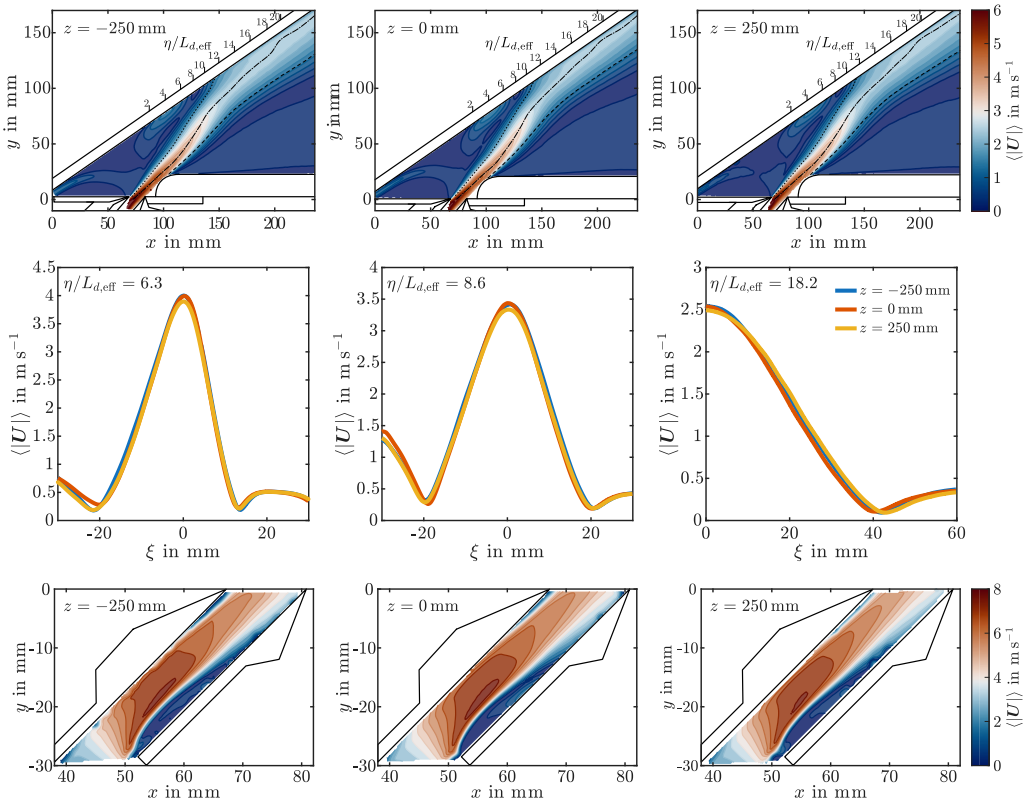

(a) ROI 2 and 3 for the windshield-attached state with $\beta = 45°$ and $L_s = 8\,\mathrm{mm}$.

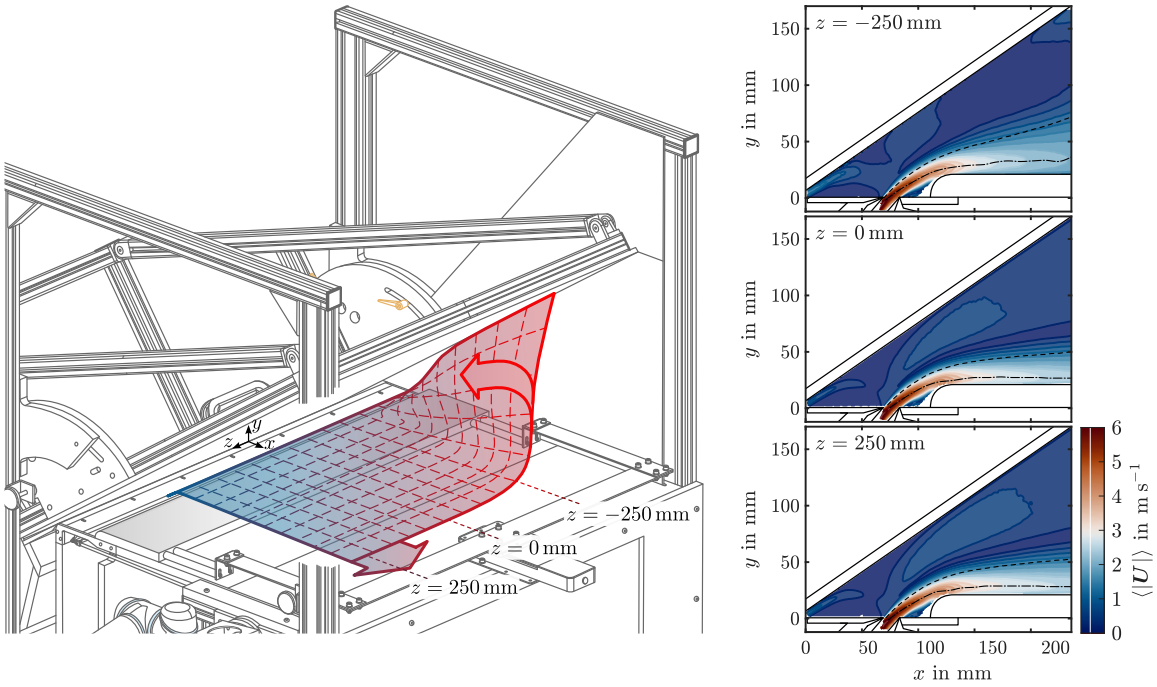

(b) ROI 2 for the dashboard-attached state with $\beta = 45°$ and $L_s = 24\,\mathrm{mm}$. An asymmetric flow pattern is noticed with respect to the spanwise direction (cf. $z = -250\,\mathrm{mm}$ with the other two positions).

Supp. Fig. 11: Results of the two-dimensionality assessment of the flow field via PIV.

4 Test Rig Photographs

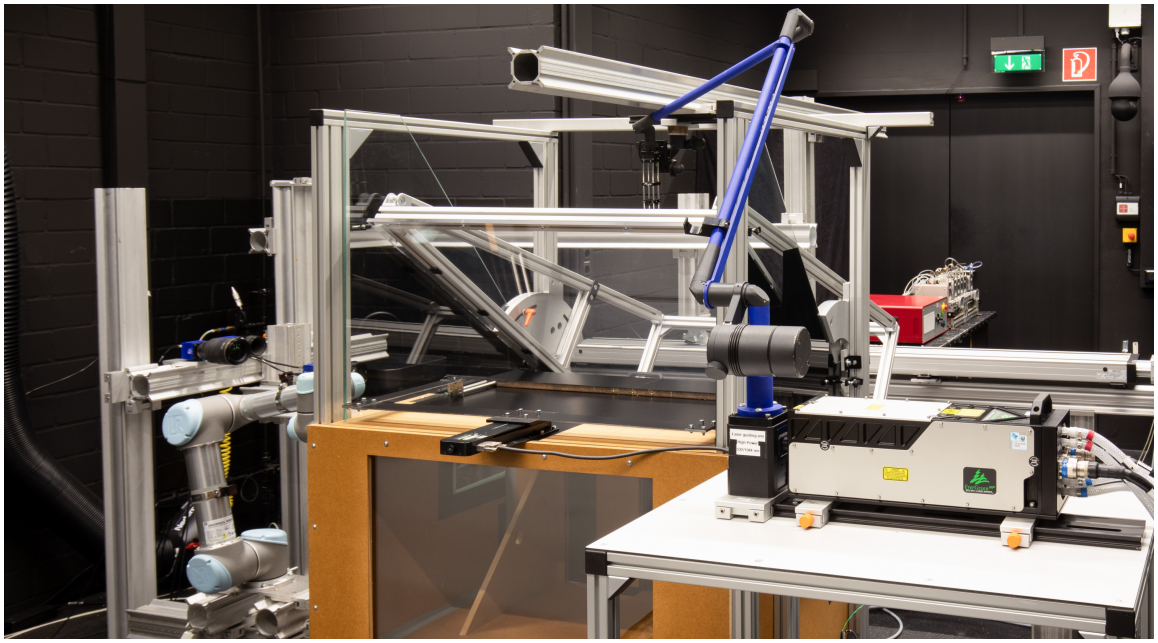

(a)

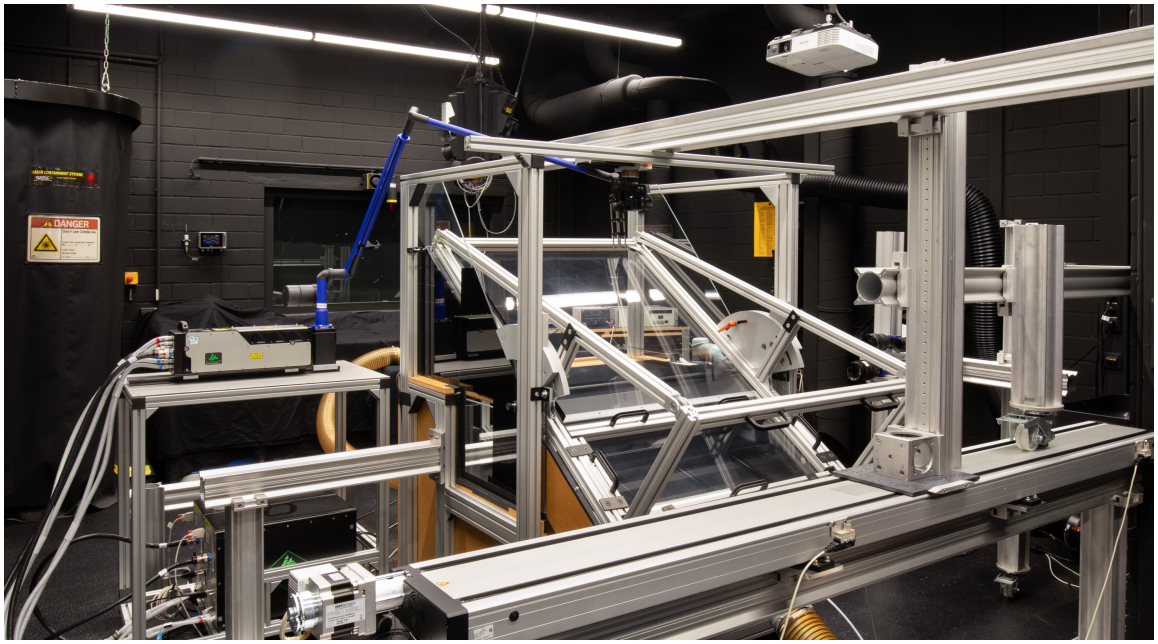

(b)

Supp. Fig. 12: Pseudo-2D defrost test rig.

References

[1] ISO16610-21:2025-01: Geometrical product specifications (GPS) - Filtration - Part 21: Linear profile filters: Gaussian filters. Standard, International Organization for Standardization (January 2025)

[2] ISO21920-3:2021-12: Geometrical product specifications (GPS) - Surface texture: Profile - Part 3: Specification operators. Standard, International Organization for Standardization (December 2021)

[3] Adams, T.M., Grant, C., Watson, H.D.: A simple algorithm to relate measured surface roughness to equivalent sand-grain roughness. In: International Journal of Mechanical Engineering and Mechatronics (2012). https://doi.org/10.11159/IJMEM.2012.008 . https://api.semanticscholar.org/CorpusID:1785401

[4] Bradshaw, P.M.D., Gee, M.T.: Turbulent wall jets with and without an external stream. Aeronautical Research Council Reports & Memoranda (1960)

[5] Eriksson, J.G., Karlsson, R.I., Persson, J.: An experimental study of a two-dimensional plane turbulent wall jet. Experiments in Fluids **25**(1), 50–60 (1998) https://doi.org/10.1007/s003480050207

[6] Gupta, A., Choudhary, H., Singh, A.K., Prabhakaran, T., Dixit, S.A.: Scaling mean velocity in two-dimensional turbulent wall jets. Journal of Fluid Mechanics **891**, 11 (2020) https://doi.org/10.1017/jfm.2020.132

List of Figures